

Characterization and origin of low-T willemite (Zn_2SiO_4) mineralization: the case of the Bou Arhous deposit (High Atlas, Morocco)

Flavien Choulet¹ · Luc Barbanson² · Martine Buatier¹ · James Richard¹ · Torsten Vennemann³ · Aomar Ennaciri⁴ · Mohamed Zouhair⁴

Received: 5 February 2016 / Accepted: 1 August 2016 / Published online: 5 September 2016
© Springer-Verlag Berlin Heidelberg 2016

Abstract Willemite (Zn_2SiO_4) usually reported in hypogene non-sulfide deposits is described as the main ore mineral in the carbonate-hosted Bou Arhous zinc deposit. This deposit is located in the High Atlas intracontinental range that formed during the Tertiary. Based on a set of microscopic observations, it was possible to establish that willemite replaces primary sphalerite. On the basis of cathodoluminescence imaging, three successive generations of willemite are distinguished, with evidence of dissolution–reprecipitation processes. Willemite is also variably enriched in Ge (up to 1000 ppm), while Ge contents lower than 100 ppm are reported in the primary sulfide minerals. Depending on the willemite generation, this substitution was positively or negatively correlated to the Zn-Pb substitution. According to the nature of zoning (sector versus oscillatory), the incorporation of Ge was either controlled by crystallographic factors or by the nature of the mineralizing fluids. Willemite is associated with other oxidation-related mineral species, like cerussite ($PbCO_3$) but is not in isotopic equilibrium and therefore not considered to be cogenetic. Oxygen isotope compositions support the formation of willemite at temperatures below 130 °C, from mixed meteoric and deeper,

hydrothermal fluids. The formation of the High Atlas Belt during the Tertiary has contributed to the exhumation of the sulfide minerals and the development of vertical conduits for percolation of meteoric water and ascending hydrothermal fluids. In addition to a local contribution of silicate minerals of the host limestone, hydrothermal fluids probably transported Si and Ge that are incorporated in willemite.

Keywords Willemite · Non-sulfide zinc ore deposit · Cathodoluminescence · Germanium · Stable isotopes · Morocco

Introduction

Unconventional non-sulfide zinc deposits have been the focus of many studies during the last two decades (e.g., Boni and Mondillo 2015). In addition to an evaluation of their economic potential, efforts have been made to establish and update the classification of non-sulfide zinc ore deposits (e.g., Hitzman et al. 2003; Boni and Large 2003). Presently, it is accepted that several types of deposits are distinguished. The supergene deposits formed by weathering of primary sulfides at surface temperature (see a review in Boni and Mondillo 2015). The hypogene deposits include (i) primary hydrothermal high-temperature zinc silicate deposits (e.g., Vazante in Brazil (Monteiro et al. 2006) or Beltana in Australia (Groves et al. 2003)); (ii) secondary metamorphosed deposits (e.g., Franklin and Sterling Hill in the USA (Johnson et al. 1990)); and (iii) secondary low-temperature (<100 °C) Zn carbonate deposits (e.g., Angouran in Iran (Boni et al. 2007; Daliran et al. 2013)).

The occurrence of willemite (Zn_2SiO_4) is generally considered to be testimony of a formation at relatively hot conditions (between 200 and 300 °C) under oxidizing and alkaline conditions (Brugger et al. 2003). However, the origin of willemite

Editorial handling: H.A. Gilg

✉ Flavien Choulet
flavien.choulet@univ-fcomte.fr

¹ Chrono-Environnement, UMR6249, Université de Bourgogne Franche-Comté/CNRS, Besançon, France

² Institut des Sciences de la Terre d'Orléans, UMR7327, Université d'Orléans/CNRS/BRGM, Orléans, France

³ Institut des Dynamiques de la Surface Terrestre, Université de Lausanne, Lausanne, Switzerland

⁴ Managem Group, Casablanca, Morocco

is controversial (Pough 1941), as the geological features of numerous willemite-rich deposits are considered to derive from low-temperature (<100 °C) hydrothermal processes or supergene weathering. The historical deposits of Belgium in the Namur-Verviers Synclinorium district include carbonate-hosted willemite ores whose origin remains disputed (Dejonghe 1998; Boni et al. 2005; Coppola et al. 2008). Based on ore characteristics and fluid inclusions, Coppola et al. (2008) hypothesized that willemite may result from low-temperature hydrothermal processes caused by oxidizing fluids with high silica activities. In addition to hypogene/hydrothermal willemite (Boni et al. 2011), supergene willemite directly replacing primary sphalerite has been described in the Namibian and Zambian carbonate-hosted oxidized zinc deposits. The crystal habits, together with the mineral association and the presence of monophasic fluid inclusions, support a meteoric origin of the mineralizing fluids or at least low-temperature hydrothermalism (Terracciano 2008). However, the presence of supergene willemite in such carbonate-hosted environments is clearly a paradox. Smithsonite (ZnCO_3) or hydrozincite ($\text{Zn}_5(\text{CO}_3)_2(\text{OH})_6$) are supposed to be stable in the weathering zone (Reichert and Borg 2008). At 25 °C, willemite may precipitate instead of smithsonite at low CO_2 fugacity ($\log f_{\text{CO}_2} < -1.6$) and in the presence of silica ($\log a_{\text{quartz}} > -3$) (Brugger et al. 2003). However, this model does not consider the possibility to precipitate hemimorphite. According to McPhail et al. (2003, 2006), hemimorphite is stable with respect to willemite at temperatures below 90–100 °C. This may explain why hemimorphite ($\text{Zn}_4\text{Si}_2\text{O}_7(\text{OH})_2 \cdot (\text{H}_2\text{O})$) is frequently reported in supergene deposits (Hitzman et al. 2003). Hence, the presence of willemite is frequently explained by the direct precipitation from low-temperature hydrothermal fluids (Coppola et al. 2008; Terracciano 2008).

Zinc silicate is a versatile luminescent mineral that has been widely used as a phosphorescent agent in displays and lighting devices (Takesue et al. 2009). Based on studies of natural Mn-rich samples from Franklin or Sterling Hill deposits, USA (Palache 1935), it has been shown that Mn^{2+} guest ions are natural luminescence activators in willemite, which emits in a green color (Bhalha and White 1972). Green willemite has been reported from hypogene deposits (Monteiro et al. 2007; Boni et al. 2011), while willemite from presumed supergene or low-temperature ores luminesces in dull to bright blue (Coppola et al. 2008; Terracciano 2008; Melcher et al. 2009). Although the origin of the blue emission is not clearly established and probably due to activator or quenching ions other than Mn^{2+} , cathodoluminescence (CL) imaging enables to reveal the different mineralization stages and may be used as a tool to discriminate the origin of willemite.

The Bou Arhous deposit in Morocco exposes a non-sulfide ore that contributed to the infilling of a large karst developed in Jurassic limestone (Leblanc 1968). The mined ore mainly

consists of willemite associated with supergene or karst-related minerals (Choulet et al. 2014, 2016). Except for the primary sulfide mineralization, no evidence of a later hydrothermal event or Si-rich fluid input has been reported yet. In this study, we present a detailed investigation of the willemite ore texture coupled with a determination of its major and trace element composition. In addition, stable isotope composition of willemite and cerussite are used to constrain the characteristics of the mineralizing fluids and discuss the origin of willemite ores.

The Bou Arhous deposit

The Bou Arhous deposit is located in the High Atlas range, in the central-eastern part of Morocco (Fig. 1a). The High Atlas range results from Tertiary intracontinental deformation related to the closure of the Tethys (Frizon de la Motte et al. 2000). The range consists of a fold-and-thrust belt with narrow anticlinal ridges and large synclinal plains. Folded units are mainly composed of Jurassic limestone and marl sequences that were originally emplaced into a horst and graben system related to the opening of the Tethyan and Atlantic oceans (Laville and Piqué 1991). Tertiary thrusts, rooted in the Triassic shales, reactivated the Jurassic normal faults. These faults delimited the horst and graben domains, characterized by contrasted sedimentary infilling.

The Moroccan High Atlas range hosts hundreds of base metal deposits and occurrences that belong to the circum-Mediterranean Zn-Pb province (Rouvier et al. 1985). Several periods of ore deposition were distinguished (Mouguina 2004; Choulet et al. 2014; Charles et al. 2016): (1) the Lower Jurassic with the emplacement of stratabound Zn-Pb-Fe sulfides, (2) the Middle Jurassic including Cu-Ni and Zn-Pb mineralization genetically associated with mafic magmatism, and (3) the Tertiary, characterized by the supergene evolution of the aforementioned Jurassic deposits. For this latter case, the supergene enrichment was strongly controlled by tectonics, which enabled the exhumation of deep sulfide lenses and the development of faults that served as drains for descending meteoric waters (Choulet et al. 2014).

Hosted in one of the High Atlas anticlinal ridges (Fig. 1b), the Bou Arhous ore deposit is enclosed in Lower Sinemurian massive limestone (l_{1-2} m), to the south of the Grand Accident Fault, a syn-sedimentary normal fault that was inverted during the Tertiary (Leblanc 1968). At the mine, the bedding is steep to vertical and even overturned (Fig. 2a). The limestone has developed a 120-m-thick karst that extends over 18,000 m^2 (Fig. 1b); sinkholes and tunnels are filled with detrital and residual clays (Buatier et al. 2016; Choulet et al. 2016). The mineralization consists of a network of interconnected vertical veins that meet the karst cavities (Fig. 2b). The width of the veins may reach up to 10 m. A vertical zonation of the

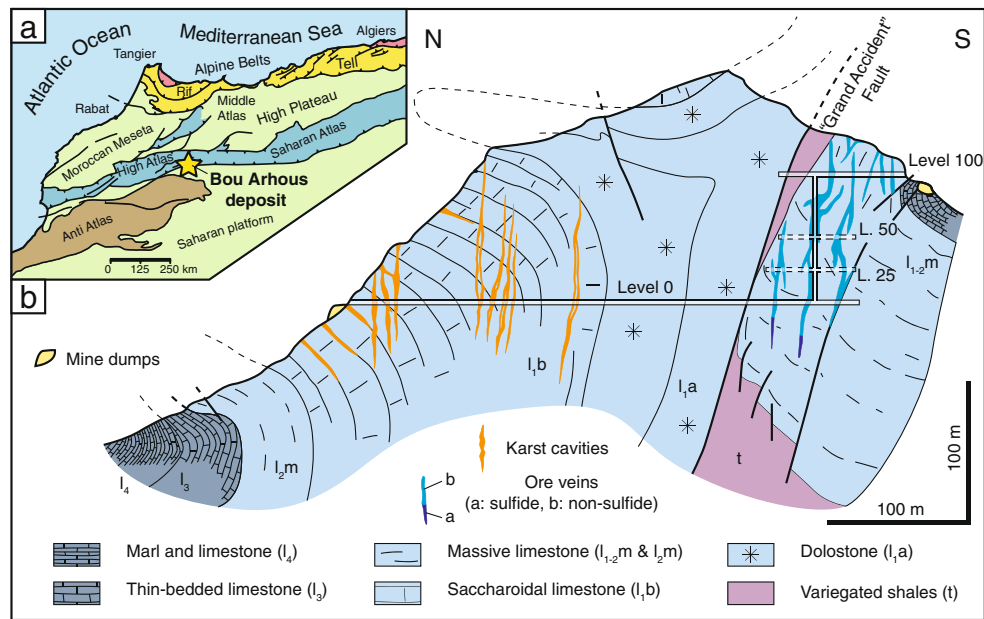


Fig. 1 a Map of northwestern Africa, illustrating the location of the Bou Arhous deposits with respect to the major tectonic features. b Cross section of the Bou Arhous deposit, showing the faulted anticline (adapted from Leblanc 1968). Triassic rocks (*t*) are covered by Lower

Jurassic rocks (*I₁* to *I₄*). The mine, made up of four levels (from level 0 to level 100) is hosted in massive limestone, to the south of the fault and mainly exposes a non-sulfide mineralization

mineralogical associations is given with preserved sulfide minerals (sphalerite and galena) at depth and newly formed non-sulfide minerals toward the surface (Choulet et al. 2014).

The Bou Arhous deposit is currently mined by Managem, and reserves have been estimated at 250 kt, grading 16 % Zn and 4 % Pb. The non-sulfide ore is mainly composed of willemite and minor smithsonite, hydrozincite, and hemimorphite. Remnant galena and cerussite are associated with willemite forming black aggregates (Fig. 2c). This black ore is often embedded in various clayey materials (Fig. 2d). The barren red clays are of residual and detrital origin, linked with the development of the karst system, whereas the white to ochre zinc clays are newly formed after willemite dissolution (Choulet et al. 2016). Ore is processed at the site of Guemassa, south of Marrakech since 2002, using hydrometallurgy to produce a ZnO concentrate as the final product. Leaching by H₂SO₄ allows zinc recovery from oxidized ores, whatever the mineralogy of the raw material (zinc silicates, carbonates, or hydrated phases but not sulfide minerals).

Material and methods

Sample preparation and microscopic observation

Hand samples of black ore were collected in the different mine levels and cut to prepare a set of 30 polished thin sections. Whole-rock powders were also used for X-ray diffraction (XRD) measurements. Procedure and results may be found

in Choulet et al. (2016). A first optical investigation using a Leica DMRX petrographic microscope was complemented by scanning electron microscopy (SEM) at the FEMTO-ST Institute (Université de Bourgogne Franche-Comté, France). Backscattered electron (BSE) imaging operated at 15 kV in low vacuum conditions was combined with semi-quantitative analysis using energy-dispersive spectrometers (EDS). Cold CL observations using OPEA instrumentation hosted at Chrono-Environnement (Université de Bourgogne Franche-Comté) were made with an acceleration voltage of 18.5 ± 1.5 keV and a current of 350 ± 150 mA to investigate zoning in willemite and establish relationships with other minerals. Additional spectral analyses were performed with a Zeiss MCS CCD UV-NIR spectrophotometer.

Micro-analyses

The major element composition of sphalerite, galena, and willemite was obtained by electron probe micro-analysis (EPMA), at the University of Lausanne, Switzerland, using a JEOL 8200 Superprobe equipped with five wavelength dispersion spectrometers (WDS). Carbon-coated polished thin sections were analyzed with a beam of 20 kV for sulfide minerals and 15 kV for willemite, respectively, and a current of 10 nA. The resolution is ca. 1 μm. Oxides, silicates, and pure metals were used as standards. Only analyses between 97 and 103 wt% were retained for discussion.

Complementary LA-ICP-MS measurements of the Ge content were made on a quadripolar Agilent 7500 ICP-

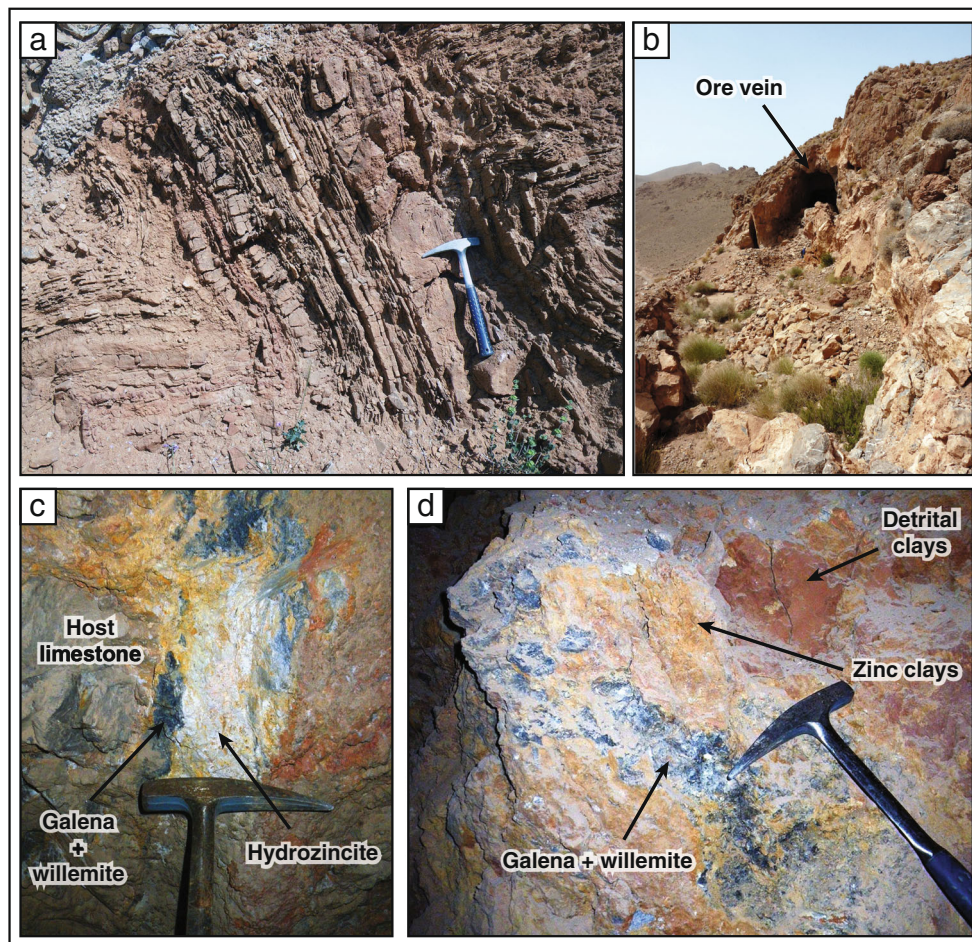


Fig. 2 **a** Field image of the reddish thin-bedded folded limestone that alternates with marl. **b** General view of the southern flank of the Jbel Bou Arhous showing cavities originally filled by non-sulfide mineralization

(Choulet et al. 2014). **c, d** Mine outcrops showing the “black ore” composed of galena and willemite, associated with zinc clays, detrital clays, or hydrozincite

MS coupled with a 193-nm excimer Resonetics M-50E laser hosted at the Université Blaise-Pascal, Clermont-Ferrand, France. The laser was set up to produce an energy density of ca. 4 J cm^{-2} at a repetition rate of 2 Hz. The laser spot size was $20 \mu\text{m}$ in diameter. The following isotopes were monitored: ^{29}Si , ^{66}Zn , ^{67}Zn , ^{68}Zn , ^{70}Ge , ^{72}Ge , ^{73}Ge , ^{74}Ge , and ^{76}Ge . The total acquisition time (background and signal) was limited to 100 s for one spot. Data reduction was carried out with Glitter software. Zinc content previously measured by EPMA was used as an internal standard. By comparing the recalculated Si and the EPMA-measured Si, it appears that ^{67}Zn is the most suitable isotope for calibration. NIST 610 and NIST 612 were used as external standards (Pearce et al. 1997). While ^{70}Ge and ^{76}Ge were not considered due to interference with ^{70}Zn and Ar isotopes, no significant differences were observed between the three other Ge isotopes. ^{72}Ge was probably underestimated because of a possible interference with $^{56}\text{Fe}^{16}\text{O}$. As the abundance of ^{74}Ge (36.28 %) largely exceeds that of ^{73}Ge (7.73 %), ^{74}Ge was retained for the quantification of Ge in willemite.

Stable isotope analyses

Stable isotope analyses of ore and host limestone were done at the University of Lausanne. Eleven willemite and seven carbonate (cerussite, calcite, and dolomite) concentrates were separated from the 200- μm milled fraction by heavy liquid methods using LST Fastfloat® liquor and filters. Grains were further handpicked under a binocular microscope. The purity of concentrates was checked by XRD, and only reflections corresponding to cerussite or willemite were observed in the respective samples. Because of the small size of the crystals, it was not possible to separate the different generations of willemite and cerussite and only bulk compositions are provided.

O_2 was extracted from willemite by using a CO_2 -laser line linked to a Finnigan MAT 253 spectrometer. Between 1.5 and 2.5 mg of sample was loaded onto a small Pt sample holder and pumped out to a vacuum of about 10^{-6} mbar. After pre-fluorination of the sample chamber, the samples were heated with a CO_2 -laser in the presence of 50 mbar of pure F_2 . Excess F_2 was separated from the O_2 produced by conversion to Cl_2 using KCl held at 150°C . The extracted O_2 was then

introduced into the inlet of a mass spectrometer. The detailed procedure may be found in Kasemann et al. (2001). Oxygen isotope compositions are given in the standard δ -notation, expressed relative to the Vienna Standard Mean Ocean Water (VSMOW) in per mil (‰). Replicate oxygen isotope analyses of the LS-1 in-house quartz standard had an average precision of ± 0.03 ‰ ($n = 5$) for $\delta^{18}\text{O}$, and all values are normalized to a value of 9.64 ‰ for NBS-28 quartz with an average accuracy better than 0.2 ‰.

The C and O isotopic composition of carbonates was determined using a GasBench II automated system interfaced to a Thermo Finnigan Delta PlusXL mass spectrometer. The procedure is adapted after Spötl and Vennemann (2003). Oxygen isotope analyses were corrected using the phosphoric acid fractionation at 70 °C for calcite (1.10087; Swart et al. 1991), for dolomite (1.0099; Rosenbaum and Sheppard 1986), and for cerussite (1.00911; Gilg et al. 2003). The data are reported in the conventional δ values as ‰ deviations relative to the Vienna Pee Dee Belemnite (VPDB) standards for C isotopes and to the VSMOW for O isotopes. Replicate isotope analyses of the in-house standard used (CM) had an average precision of ± 0.04 ‰ for $\delta^{13}\text{C}$ and ± 0.07 ‰ for $\delta^{18}\text{O}$ ($n = 4$).

Results

Host rock and ore characterization

The host rock of the Bou Arhous mineralization is a massive fine-grained gray to bluish-gray limestone. This micritic limestone locally includes coarse fragments of echinoderms and lamellibranchs (Leblanc 1968). Idiomorphic quartz crystals are frequently found in the micritic limestone as well as secondary sparite (Fig. 3a). Despite a general euhedral shape, quartz grains often display a skeleton-like aspect, suggesting dissolution (Fig. 3a), with evidence of late sparite precipitated in the newly formed porosity. In addition, the bulk composition of the massive limestone has high MgO contents (up to 13 wt%) that can be explained by a pervasive dolomitization also revealed by XRD patterns (Choulet et al. 2016). Cathodoluminescence imaging shows large dolomite crystals luminescing red within the micrite (Fig. 3b). In some cases, dolomite may be altered and replaced by calcite. Small cavities or sinkholes are filled with sparite with yellow luminescence (Fig. 3c). At the edge of the cavity, an accumulation of dolomite rhombs and idiomorphic quartz is observed (Fig. 3c). This stack of insoluble minerals differs from their random distribution in the preserved micritic facies.

According to the XRD results, the ore is composed of willemite, cerussite, galena, and clays, associated with calcite, quartz, and dolomite from the gangue and the host rocks (Choulet et al. 2014, 2016). Remnant sulfide minerals include

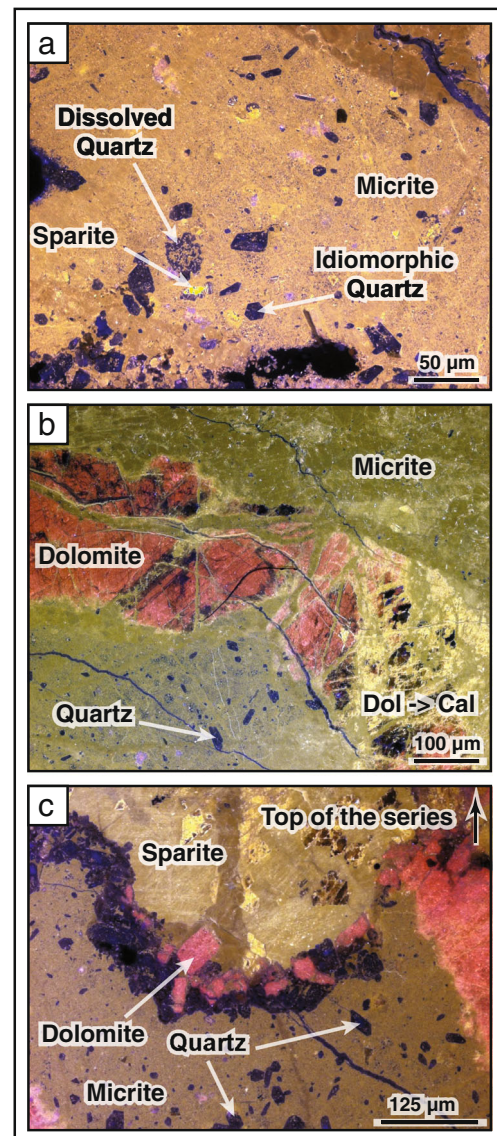


Fig. 3 Cathodoluminescence images of the host limestone. **a** Micrite (yellowish pink) enclosing idiomorphic and partly dissolved quartz (blue), with locally secondary sparite (yellow). **b** Dolomite (reddish pink) pervading into the micrite (yellowish brown) and locally transformed into sparite (yellow). **c** Small sinkhole formed after the dissolution of micrite (brown) and filled by sparite (yellow). Note the accumulation of euhedral crystals of dolomite (pink) and quartz (blue) at the bottom of the cavity

sphalerite and galena. In thin sections, corroded sphalerite can be seen as embedded in willemite (Fig. 4a, g) and secondary galena (Gn II) has precipitated onto the rim of partly dissolved sphalerite or along fractures cutting euhedral sphalerite (Fig. 4b, h). Like the host micrite, willemite includes idiomorphic quartz crystals, exposing fractures and evidence of corrosion (Fig. 4b). An irregular rim of anglesite locally coats the galena (Gn I) and is itself transformed into cerussite (Fig. 4c). Frequently, only granular cerussite that armors galena is observed and this assemblage often constitutes the core of the euhedral willemite crystals (Fig. 4d, e). This latter type of

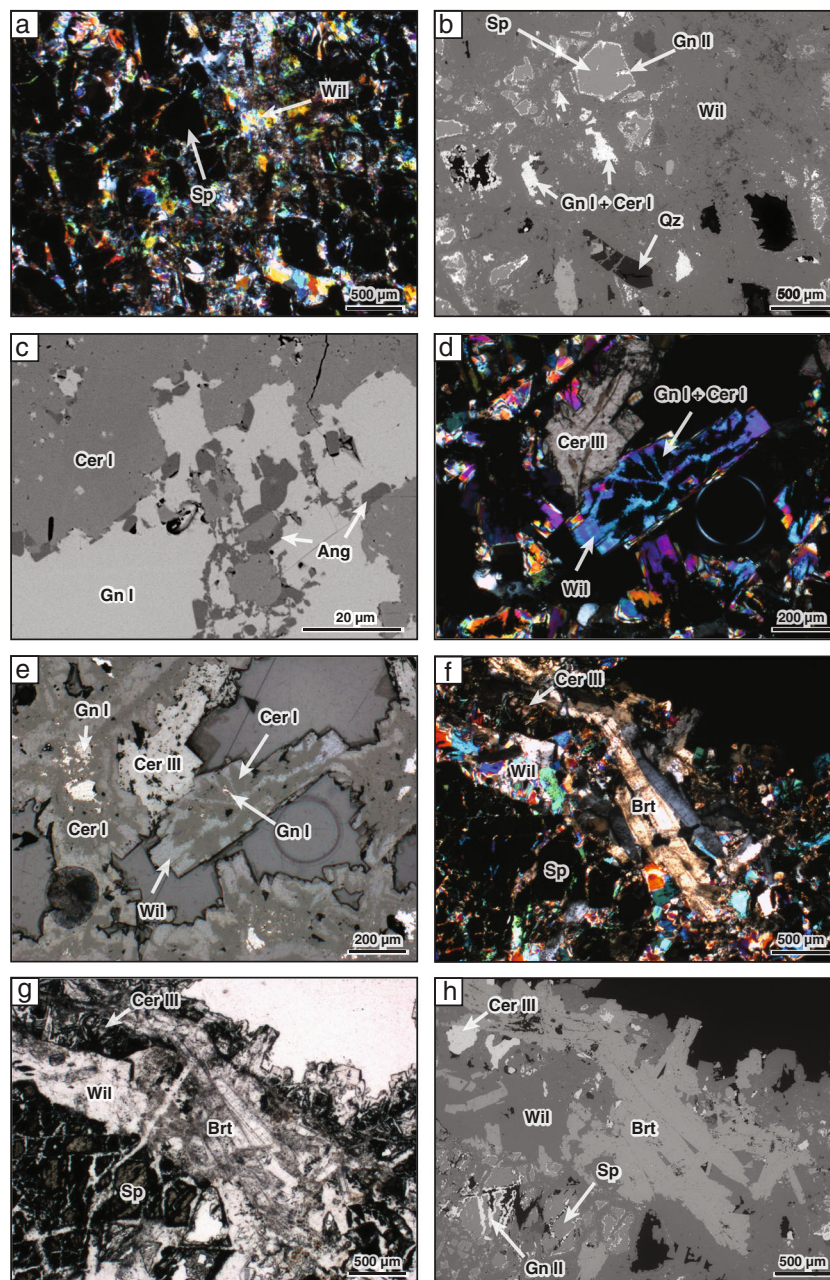


Fig. 4 Images of the ore mineralization. **a** General view (TL, nic+) of the willemite (*Wil*) ore including relics of sphalerite (*Sp*) (sample BA06C). **b** BSE image of **a** showing sphalerite relic rimmed by secondary galena (*Gn II*), within willemite. Note the idiomorphic quartz (*Qz*) crystals, partly corroded and fractured. **c** BSE image of primary galena (*Gn I*) coated by a thin rim of anglesite (*Ang*) itself transformed into cerussite (*Cer I*) (sample BA05A). **d** (TL, nic+), **e** (RL, nic//) Aggregates of galena and cerussite (*Cer I* + *Gn I*) included within elongated willemite (*Wil*)

crystals (sample BA06B). Large crystal of cerussite (*Cer III*) devoid of galena inclusions fills the porosity between the willemite (*Wil*) aggregates. **f** (TL, nic+), **g** (TL, nic//), and **h** (RL, nic//) Thin and tabular barite (*Brt*) crystals associated with willemite (*Wil*), late cerussite (*Cer III*), and sphalerite (*Sp*) rimmed by secondary galena (*Gn II*) (sample BA06A). *TL* transmitted light, *BSE* backscattered electron, *RL* reflected light, *nic+* crossed nicols, *nic//* parallel nicols

cerussite (*Cer I*) must not be mistaken for the late tabular crystals of cerussite (*Cer III*) observed in the druses (Fig. 4e). Clusters of thin tabular crystals of barite are found in association with willemite and cerussite (Fig. 4f–h) or as late overgrowths within the geodes. Two types of willemite crystals have been found in all thin sections. While small

barrel-shaped crystals are found in the equigranular ore facies (Fig. 4d), radial-fibrous aggregates locally form a botryoidal facies (Fig. 5a). In both cases, willemite crystals may display an irregular outline suggesting dissolution, with zinc clays growing over willemite and filling the newly formed porosity (Fig. 5b). These clay minerals associated with detrital quartz

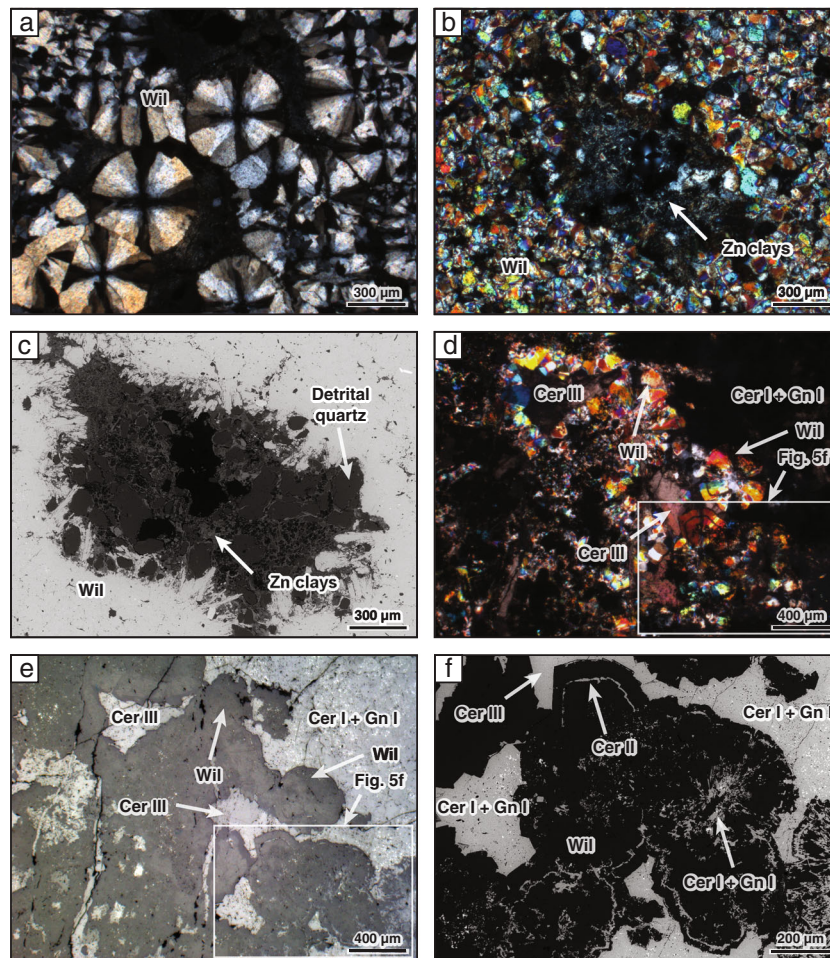


Fig. 5 **a** Aggregate of willemite spherulites in the massive ore facies (TL, nic+) (sample BA135F). **b** (TL, nic+), **c** (BSE image) Association of willemite with newly formed zinc clays and detrital quartz, extensively described in Choulet et al. (2016) (sample BA130F). **d** (TL, nic+), **e** (RL, nic//) General view of the different generations of cerussite and

relationships with the willemite spherulite (sample BA05B). **f** BSE image illustrating willemite spherulites postdating early cerussite (cer I associated with primary galena relic) and predating late cerussite (cer III). Note the cerussite band (cer II) intercalated during the growth of the spherulite. See Fig. 4 for abbreviations

(Fig. 5c) correspond to the white clayey material that encompasses the willemite ore (Fig. 2d); they were described in detail by Buatier et al. (2016) and Choulet et al. (2016). Radial-fibrous willemite aggregates seem to postdate early cerussite (Cer I, often associated with Gn I) and predate late cerussite infilling (Cer III, without galena) (Fig. 5d, e). In addition, cerussite (Cer II) bands are intercalated between the different stages of willemite growth (Fig. 5f).

As outlined above, several morphotypes of willemite may be found. This includes (1) idiomorphic barrel-shaped crystals (Fig. 6a), which are frequently twinned (Fig. 6b) and (2) radial-fibrous aggregates or spherulites (Fig. 6c, d). These crystal types must not be confused with the successive generations of willemite that are described in the following section.

Identification of willemite generations

CL imaging was used for deciphering the successive generations of willemite. The Bou Arhous willemite luminesces in

blue from dull indigo to bright greenish-blue. Three successive generations were distinguished:

- Willemite Ia (Wil Ia), which partly refers to the prismatic morphotype (Fig. 6a) is characterized by sectoral zoning with sectors identified by their luminescence (Fig. 7a). Deep indigo sectors seem to be associated with particular faces, while bright blue sectors correspond to other faces. When crystals display penetration twinning, pseudo-patchy zoning with an irregular dark and bright chessboard pattern is observed. The extreme stage of multiple twinning corresponds to the second morphotype of willemite, spherulites (Fig. 6c, d), which exhibit a radial distribution of triangular dark sectors separated by thin bright sectors (Fig. 7b).
- Willemite Ib (Wil Ib) exhibits well-defined oscillatory zoning characterized by a fine alternation of bright blue and dark indigo bands (Fig. 7b). Wil Ib always develops on a core crystal, usually Wil Ia, with a sharp transition from sectoral to oscillatory zoning (Fig. 7a, b). Individual

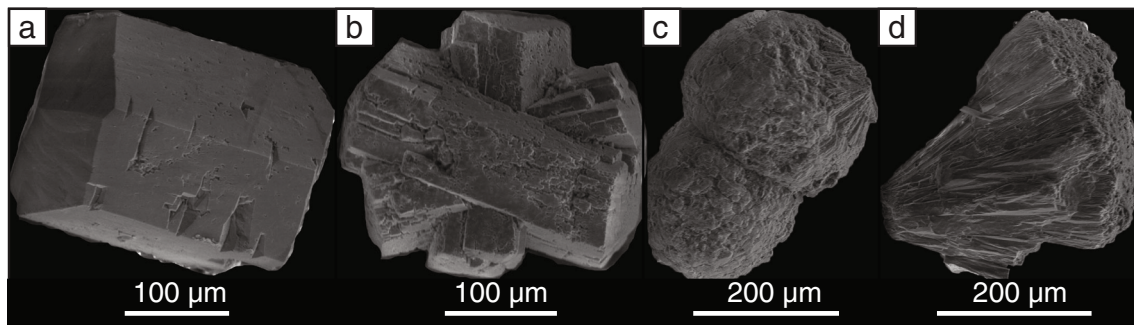


Fig. 6 Secondary electron images of separated willemite crystals, showing idiomorphic barrel shape (a) (sample BA124), twinning (b) (sample BA133), and radial-fibrous distribution (c and d) (sample 134)

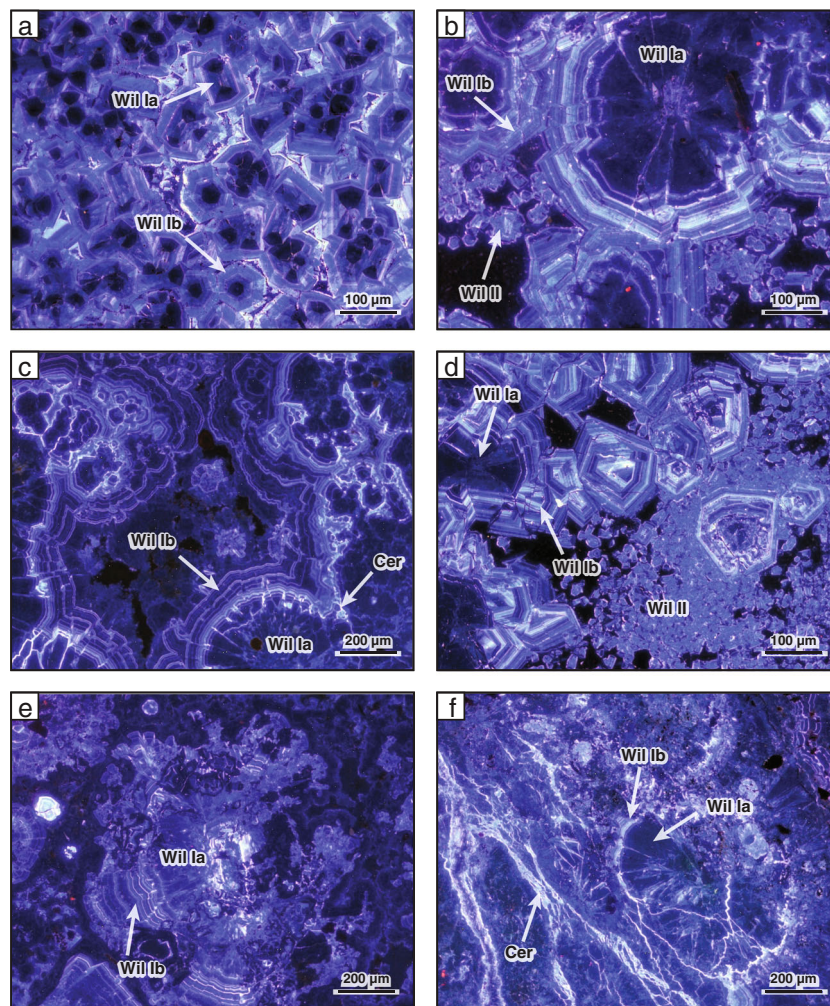


Fig. 7 Cathodoluminescence images of the willemite ore. **a** Barrel-shaped crystals showing a (1) core of Wil Ia with sector zoning and (2) a rim of Wil Ib with oscillatory zoning (sample BA130). **b** Willemite spherulite composed by a core of Wil Ia mainly composed of dark sectors, rimmed by oscillatory-zoned Wil Ib (sample BA135F). **c** Aggregated spherulites showing a well-developed Wil Ib stage (sample BA128F). Note the cerussite veins (*bright white-blue*) that crosscut Wil Ia and partly Wil Ib. **d** Small crystals of late willemite (*Wil II*) filling the porosity

between early willemite (*Wil Ia* and *Wil Ib*) (BA135). **e** Partly dissolved willemite, exposing relics of an oscillatory-zoned rim and dark sectors within the core. The bright zone in the center is due to early cerussite (sample BA128F). **f** Partly dissolved willemite spherulite crosscut by cerussite veinlets (*bright white-blue*). Note on the *upper right corner* that the sequence is probably repeated with time, as unaltered willemite with oscillatory zoning overgrows on the dissolved spherulites (sample BA128F)

- willemite spherulites may be merged to form aggregates, rimmed by banded willemite (Fig. 7c).
- Willemite II (Wil II) corresponds to small grains that precipitate in the pores between the aggregates of banded willemite or the willemite spherulites (Fig. 7d). They systematically form after a major dissolution stage affecting both Wil Ia and Wil Ib, as evidenced by the convolute or truncated shape of crystals (Fig. 7e, f). This dissolution stage is accompanied by the pervasive development of thin interconnected fractures filled with cerussite (Fig. 7c, f) that luminesces in bright bluish white.

Composition of sulfide minerals and willemite

The mineral compositions of sulfides (galena and sphalerite) were obtained by EPMA and are given in Table 1. Sphalerite is poor in Fe (<0.1 wt%), and minor elements were not detected. For galena, the minor element content is low except for Ag, which may reach up to 0.3 wt%.

The composition of the different generations of willemite was obtained by EPMA and LA-ICP-MS methods, and results are reported in Table 2. The total oxide content averages 99 wt%, with a standard deviation between 0.3 and 0.6 wt%. The major oxide content (ZnO and SiO₂) slightly varies (1 to 2 wt%) between the different generations of willemite (Table 2). Willemite does not contain major impurities, except for PbO that may reach up to 2 wt% (Table 2). No Mn was detected in the different generations of willemite. The Ge content analyzed by LA-ICP-MS was compared to the Ge content recalculated from EPMA-measured GeO₂. Despite slight differences, both datasets have the same trend and a similar range of element

contents. Significant differences between willemite sectors distinguished by CL imaging may be noticed. While the dark sectors of Wil Ia have a low Ge content (less than 200 ppm) and a high PbO content (up to 2 wt%), the light sectors have significant Ge contents with up to 1100 ppm (Fig. 8a, b). In both cases, the relative standard deviation is low (Table 2). In contrast, the values for Ge in Wil Ib are irregularly distributed with a range from 22 to 858 ppm and high standard deviation (Table 2). Ablation spots were too large, compared to the growth bands of oscillatory-zoned crystals (Fig. 8b). But, using EPMA, it was possible to analyze each band, and no direct connection between the Ge content and the luminescence of the Wil Ib crystals is observed. The range for PbO content is between 0.06 and 0.84 wt% (Table 2). For Wil II, the Ge content is below the detection limit and the PbO content ranges are similar to those of other willemite generations.

In the individual Wil Ia crystals, a correlation between the Ge and Si contents is marked by an extremely well-constrained trend line with a negative slope (Fig. 8c, d). Despite an apparent random distribution, a similar trend is observed for all data from Wil Ia and Wil Ib crystals (Fig. 8e). The Ge enrichment in willemite is accompanied by a lower concentration of Si. When comparing the Zn and Pb contents, differences between the different types of willemite are noted. While there is no apparent correlation between Zn and Pb for Wil Ib, a well-defined trend with a negative slope is observed for Wil Ia and Wil II (Fig. 8f).

Stable isotope compositions

Results of the stable isotope analyses on bulk willemite, bulk cerussite, and host carbonate samples are given in Table 3. For

Table 1 WDS results of the primary sulfide minerals (sphalerite and galena)

Sample	BA06A				BA06A				BA06A			
Type	Sphalerite <i>n</i> = 7				Sphalerite <i>n</i> = 14				Galena <i>n</i> = 15			
	Range	Avg.	SD	RSD	Range	Avg.	SD	RSD	Range	Avg.	SD	RSD
S	31.91–32.85	32.37	0.34	1	31.33–32.5	32.16	0.29	1	12.27–12.58	12.44	0.1	1
Cd	0.23–0.31	0.27	0.03	10	0.23–0.43	0.29	0.05	17	0.05–0.12	0.08	0.02	23
As	0–0.12	0.04	0.04	105	0–0.12	0.03	0.04	150	0–0.04	0.01	0.01	102
Bi	–	–	–	–	–	–	–	–	–	–	–	–
Fe	0.04–0.07	0.05	0.01	19	0.04–0.21	0.09	0.04	39	0–0.02	0.01	0.01	142
Ag	0–0.06	0.02	0.02	119	0–0.15	0.04	0.05	139	0–0.29	0.04	0.09	230
Ni	0–0.02	0.01	0.01	94	0–0.02	0.01	0.01	115	0–0.02	0.01	0.01	172
Zn	65.1–66.44	65.85	0.49	1	65.12–66.52	65.878	0.4	1	0–0.03	0.01	0.01	142
Pb	–	–	–	–	–	–	–	–	86.32–87.43	86.91	0.38	1
Ge	–	–	–	–	–	–	–	–	–	–	–	–
Cu	0–0.1	0.01	0.01	96	0–0.1	0.01	0.02	175	0–0.03	0.01	0.01	134
Σ	97.8–99.54	98.63	0.52	0.53	97.08–99.20	98.51	0.59	0.59	98.91–100.02	99.5	0.38	0.38

Detection limits (in ppm): S (320), Cd (100), As (210), Bi (900), Fe (110), Ag (460), Ni (120), Zn (330), Pb (720), Ge (100), Cu (110)
 Avg. average, SD standard deviation, RSD relative standard deviation (RSD = (SD / Avg.) × 100), *n* number of analyses, (–) values below the detection limit

Table 2 WDS analyses (oxide in weight percent) and LA-ICP-MS results (in ppm) of the different willemite generations described in the text

Generation	Wil Ia (dark sectors) <i>n</i> = 15				Wil Ia (light sectors) <i>n</i> = 5			
	Range	Avg.	SD	RSD	Range	Avg.	SD	RSD
SiO ₂	27.29–28.36	27.89	0.31	1	27.12–27.60	27.37	0.17	1
GeO ₂	0–0.05	0.03	0.01	33	0.04–0.13	0.10	0.03	30
Al ₂ O ₃	0–0.07	0.04	0.02	50	0–0.02	0.01	0.01	100
ZnO	68.46–71.76	70.26	0.88	1	70.62–71.32	71.09	0.22	0
PbO	0.07–1.91	0.88	0.49	56	0.30–0.81	0.57	0.16	28
CdO	0–0.01	0.01	<0.01	–	0–0.01	0.01	<0.01	–
FeO	0–0.08	0.04	0.02	50	0–0.03	0.03	<0.01	–
CaO	0–0.05	0.02	0.01	50	0–0.03	0.02	0.01	50
MnO	0–0.04	0.04	<0.01	–	–	–	–	–
Total	97.75–100.31	99.11	0.60	1	98.78–99.54	99.16	0.28	0
Generation	Wil Ia (dark sectors) <i>n</i> = 5				Wil Ia (light sectors) <i>n</i> = 9			
	Range	Avg.	SD	RSD	Range	Avg.	SD	RSD
Ge ⁷⁴	108–316	177	82	46	825–1108	941	89	9
Generation	Wil Ib <i>n</i> = 11				Wil II <i>n</i> = 5			
	Range	Avg.	SD	RSD	Range	Avg.	SD	RSD
SiO ₂	27.15–28.32	27.71	0.33	1	27.75–28.69	28.32	0.32	1
GeO ₂	0–0.13	0.06	0.04	67	0–0.01	0.01	<0.01	–
Al ₂ O ₃	0–0.06	0.03	0.02	67	0–0.09	0.04	0.03	75
ZnO	70.03–71.68	70.84	0.49	1	69.92–71.33	70.74	0.58	1
PbO	0.06–0.84	0.26	0.21	81	0.11–1.20	0.56	0.45	80
CdO	0–0.01	0.01	<0.01	–	–	–	–	–
FeO	0–0.04	0.03	<0.01	–	0–0.06	0.06	<0.01	–
CaO	0.01–0.07	0.03	0.01	33	0–0.03	0.02	<0.01	–
MnO	0–0.07	0.07	<0.01	–	0–0.04	0.04	<0.01	–
Total	98.26–99.85	98.93	0.51	1	98.90–100.02	99.71	0.43	0
Generation	Wil Ib <i>n</i> = 3							
	Range	Avg.	SD	RSD				
Ge ⁷⁴	22–858	365	347	95				

Detection limits (in ppm): Ge (84), Al (64), Pb (454), Cd (105), Fe (237), Ca (120), and Mn (336)

Avg. average, *SD* standard deviation, *RSD* relative standard deviation ($RSD = (SD / Avg.) \times 100$), *n* number of analyses, (*n.d.*) values below the detection limit

willemite, $\delta^{18}\text{O}$ values range from 5.3 to 7.8 ‰, except for sample BA136 ($\delta^{18}\text{O} = 15.6$ ‰) that was contaminated by the in-house quartz standard during laser extraction. While the $\delta^{18}\text{O}$ values of cerussite are between 11.6 and 12.9 ‰, those of the limestone range from 22.9 to 24.1 ‰. Similarly, cerussite has low $\delta^{13}\text{C}$ values with a high variance (–11 to –15.1 ‰), while the $\delta^{13}\text{C}$ values of host carbonates are between –1.7 and 1.4 ‰.

Discussion

Significance of the different willemite generations

Textures support three successive generations of willemite, with differences in crystal shape, CL zoning, and chemical

composition. While idiomorphic Wil Ia is characterized by sector zoning, radial-fibrous aggregates of Wil Ib have oscillatory zoning and growth bands (Fig. 7). This textural evolution recalls that of the willemite from ore deposits in Namibia, Zambia (Terracciano 2008), or Belgium (Coppola et al. 2008), where two distinct forms of willemite agglomerates were distinguished. These authors described (1) idiomorphic hexagonal crystals and (2) massive spheroids with radial-fibrous crystals, which are very similar to Wil Ia and Wil Ib observed at Bou Arhous, respectively. In the case of willemite, crystal shape is strongly controlled by temperature (Palache 1935; Pough 1941) and by the degree of supersaturation (Kostov 1968). Although accurate temperature constraints are missing, Kostov (1968) has proposed that, at high temperature, crystals are usually tabular and as temperature decreases, they tend to form elongated prisms along the *c* axis and, for extreme cases,

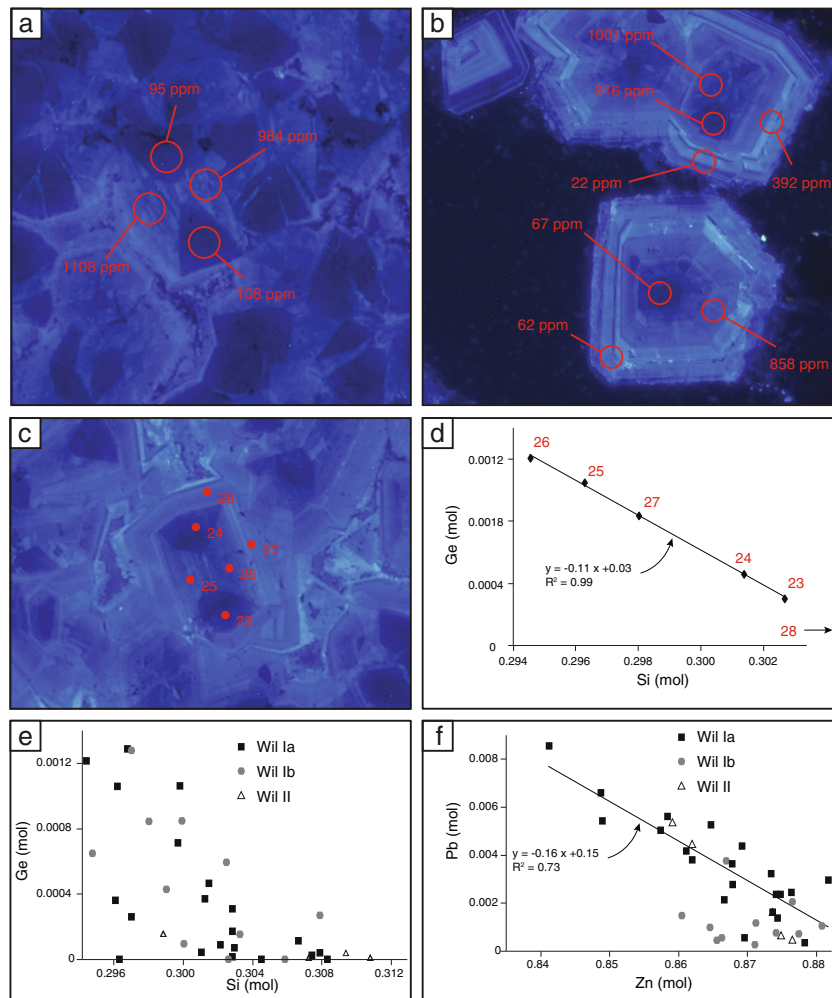


Fig. 8 Cathodoluminescence images of the willemite crystals, showing the location of in situ point analyses by LA-ICP-MS (**a**, **b**) and by EPMA (**c**). **d** Ge versus Si plot of individual EPMA analyses located in Fig. 8c. **e** Ge versus Si plot of all EPMA analyses, including the distinguished

willemite generations. **f** Pb versus Zn plot of all EPMA analyses, including the distinguished willemite generations. The number of Ge, Si, Zn, and Pb moles was calculated from the weighted percent oxide compositions reported in Table 2

radial agglomerates of fibers. Kostov (1968) also proposed that a slow crystallization from slightly supersaturated solutions could explain the short-prismatic to tabular habits.

Based on a detailed microscopic observation of ore samples, we established the temporal sequence of mineralization at Bou Arhous (Fig. 9). Primary sulfide mineralization follows or at least overlaps the dolomitization and the silicification. The latter alteration is marked by the development of authigenic quartz crystals in the micritic limestone. Such quartz is usually found in carbonates affected by saline or hypersaline pore waters (Flügel 2010); at Bou Arhous, the pore waters, from which the authigenic quartz crystals precipitated, may result from the influence of the underlying Triassic evaporites (Leblanc 1968). Cerussite predates and postdates willemite precipitation (Fig. 9), as it may be found as core inclusions and cementing material (e.g., Figs. 4d and 5e). Intercalation of cerussite bands within growth-zoned willemite (Fig. 5f) supports the contemporaneity of both phases.

Dissolution of willemite was probably caused by a change in the local hydrochemical conditions (i.e., Si-undersaturated fluids, change of temperature) and resulted in the release of zinc and silica into the solutions, contributing to either a precipitation of a new generation of willemite (Wil II) or the formation of authigenic zinc clays (Buatier et al. 2016; Choulet et al. 2016).

Incorporation of Ge in willemite with implications for cathodoluminescence properties

Both EPMA and LA-ICP-MS analyses indicate a variable Ge content in willemite that may reach up to 1000 ppm (Table 2). These values are significantly higher than those measured in the New Jersey deposits (less than 10 ppm; Höll et al. 2007) and in the Utah and New Mexico deposits (up to 350 ppm; Sheffer 1966) but are comparable to those reported from the Tsumeb Ge deposit, Namibia (up to 1280 ppm; Lombaard

Table 3 Stable isotope (C, O) compositions measured for cerussite, willemite, and host limestone from the Bou Arhous deposit

Bulk cerussite			
Sample	$\delta^{13}\text{C}$ VPDB	$\delta^{18}\text{O}$ VSMOW	
BA117	-11.0	12.9	
BA118	-13.3	11.6	
BA134	-14.5	11.9	
BA153	-15.1	12.7	
Host carbonates			
Sample	$\delta^{13}\text{C}$ VPDB	$\delta^{18}\text{O}$ VSMOW	
BA147	-1.7	23.4	
BA158	1.4	24.1	
BA159	-1.0	22.9	
Bulk willemite			
Sample	$\delta^{18}\text{O}$ VSMOW	$\delta^{18}\text{O}$ VSMOW _f ¹	$\delta^{18}\text{O}$ VSMOW _f ²
BA117	7.8	-7.4	2.0
BA118	5.9	-9.3	0.1
BA124	5.3	-9.3	-0.5
BA128	5.9	-9.3	0.1
BA130	7.2	8.0	1.4
	7.0	-8.1	1.2
BA131	7.3	-7.8	1.5
BA133	6.9	-8.2	1.1
BA134	7.4	-7.8	1.6
BA135	6.4	-8.8	0.6
BA136 ^a	<i>12.7</i>	-2.5	6.9
	<i>12.5</i>	-2.7	6.7
BA138	6.2	-9.0	0.4

Data in italics were not used for the discussion

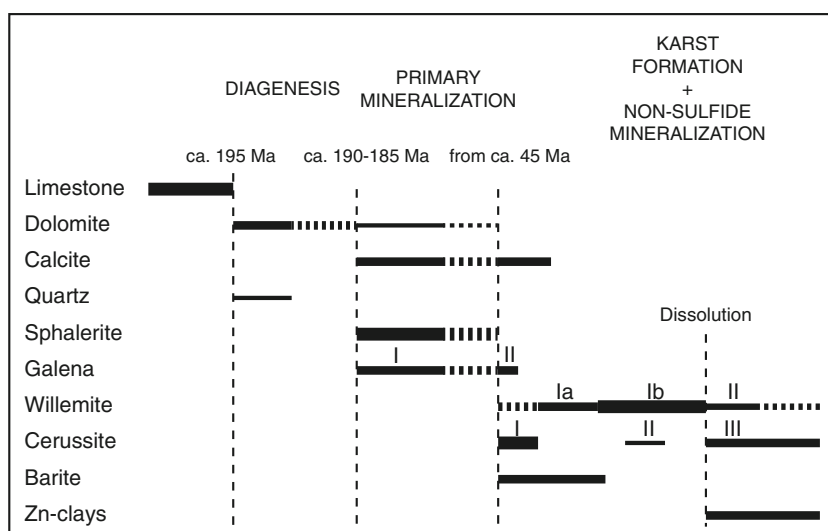
For willemite, the oxygen isotopic composition of the fluid ($\delta^{18}\text{O}$ VSMOW_f) was calculated with the fractionation equation from Zheng (1993), assuming temperatures of 25 (¹) and 100 °C (²)

^aBA136 contains a small proportion of quartz

et al. 1986) or Tres Marias Zn-Pb-(Ge) deposit, Mexico (up to 4000 ppm; Saini-Eidukat et al. 2009, 2016). The EPMA results of this study clearly show a correlation with a negative slope between Si and Ge, explained by the Ge-Si substitution within willemite (Fig. 8d, e). X-ray absorption fine structure (XAFS) spectroscopy has confirmed that Ge in willemite occurs as Ge⁴⁺ (Melcher et al. 2009; Saini-Eidukat et al. 2016). The lithophile behavior of germanium (Bernstein 1985), the short difference in ionic radii between Ge⁴⁺ (0.44 Å) and Si⁴⁺ (0.39 Å), and the similarity of lattice parameters between Zn₂SiO₄ and Zn₂GeO₄ (Hang et al. 1970) may explain the incorporation of Ge into willemite.

Generally, sulfide minerals like sphalerite (e.g., Cook et al. 2009; Bélistont et al. 2014) and galena (Monteiro et al. 2006) may contain several thousands of parts per million of Ge. At Bou Arhous, the Ge content of the two sulfide minerals is below the detection limit (100 ppm) of EPMA (Table 1), in agreement with the low Ge content of MVT deposits (Höll et al. 2007). Although the limited amount of sphalerite and galena relics precludes implication for the whole primary mineralization, it means that either an exceptional secondary Ge enrichment is recorded within willemite or that the sulfide minerals were not the source of Ge. Except for the Apex mine where Ge grades (ca. 5000 ppm) in the weathering zone exceed those in the primary sulfides (650 ppm; Bernstein 1986), the oxidation zones of Zn-Pb sulfide deposits are generally depleted in Ge or at least not enriched (Höll et al. 2007). In the Tres Marias Deposit (Saini-Eidukat et al. 2009), the Ge content of sphalerite averages 960 ± 515 ppm and is comparable to that of willemite (941 ± 89 ppm). Ge can be transported in aqueous hydrothermal fluids as Ge(OH)₄^o(aq) at pH values <8 over a temperature range of 20 to 350 °C (Pokrovsky et al. 2005). In addition, the solubility of Ge in thermal waters increases with temperature and salinity

Fig. 9 Synthetic paragenetic sequence of the observed minerals at the Bou Arhous deposit. Vertical lines represent the limits between the different steps that contribute to the present-day mineralization. Thickness of the horizontal line corresponds to the relative abundance of each mineral species



(Melcher et al. 2003). In this case, the source of Ge could be organic-rich rocks (e.g., black shale), which are generally rich in Ge (Bernstein 1985) and are frequent in the Paleozoic basement of Morocco (Lüning et al. 2000). Hydrothermal fluids would therefore be necessary to introduce the Ge for the willemite.

In addition to Ge, willemite has a variable Pb content that may reach up to 2 wt%, similar to the contents measured in Tres Marias willemite (Saini-Eidukat et al. 2009). By plotting Pb versus Zn, a correlation with a negative slope between both elements is given, suggesting the existence of a Zn-Pb substitution (Fig. 8f), also reported by Saini-Eidukat et al. (2016). According to XAFS spectroscopy, Pb is present as Pb^{2+} in willemite (Melcher et al. 2009; Saini-Eidukat et al. 2016). Willemite containing ca. 0.5 wt% of Pb^{2+} was synthesized by the sol-gel method with calcination at 1000 °C (Yang et al. 2004). Trigonal willemite is characterized by ZnO bonds (Kostov 1968); as the difference between the ionic radii of Zn^{2+} (0.60 Å) and Pb^{2+} (0.98 Å) is huge, only a limited amount of Pb^{2+} may be introduced, with strong distortion of the tetrahedrally coordinated site. Alternatively, the ring crystal structure of willemite is characterized by tessellated hollow hexagons made of Si and Zn tetrahedrons (Klaska et al. 1978; Lukić et al. 2008), which may incorporate interstitial ions like Pb^{2+} (Yang et al. 2004). The relative incompatibility of Pb in willemite is also shown by the existence of orthorhombic larsenite (Palache 1928; Ito and Frondel 1967), $ZnPbSiO_4$, and the absence of solid solution between larsenite and willemite. Hence, Saini-Eidukat et al. (2016) have proposed that Pb-rich willemite may contain microdomains of larsenite. In case of Pb supersaturation conditions related to a change of the fluid composition, secondary galena or cerussite may be precipitated (Terracciano 2008), as illustrated by the cerussite and galena inclusions in willemite cores (Fig. 4d, e) and the intercalated cerussite bands (Fig. 5f).

Correlations between the two substitutions (Zn-Pb and Si-Ge) can be observed, depending on the willemite generations (Fig. 10). In the case of Wil Ia, all data except those with low Pb and low Ge contents are distributed along a trending curve with a negative slope, which tends toward the Pb-rich compositions of willemite. This indicates that significant Ge amounts can be included in this particular willemite generation, only if that latter one is poor in Pb. As the Pb content increases, the Ge-Si substitution is much more limited, probably due to the distortion of the tetrahedrally coordinated site caused by the introduction of large Pb^{2+} ions (Saini-Eidukat et al. 2016). In contrast, for Wil Ib, the curve has a positive slope, suggesting that there is no competition between the two substitutions (Fig. 10). This trend is similar to that of Tres Marias willemite, which is also characterized by well-developed oscillatory zoning (Saini-Eidukat et al. 2009, 2016). In the case of Wil II, the small number of data and the low Ge content preclude discussing incorporation mechanisms. The differences

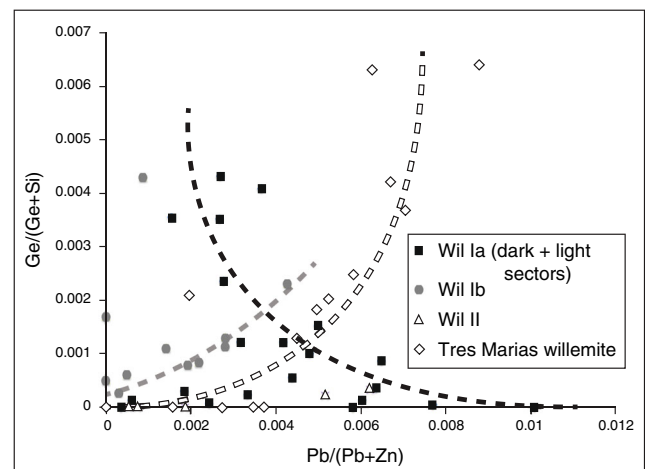


Fig. 10 Ge/(Ge + Si) versus Pb/(Pb + Zn) plot illustrating that the two substitutions (Ge-Si and Pb-Zn) are variably correlated depending on the willemite generation. The data from willemite of Tres Marias deposit, Mexico (Saini-Eidukat et al. 2009) are reported for comparison; these latter data show a trend similar to that of Wil Ib from Bou Arhous

between Wil Ia and Wil Ib may be explained by the variation of crystal shapes (prismatic versus fiber-like) and, in the case of Wil Ia, by the development of peculiar faces, which may incorporate more or less Ge and Pb at the their surface during crystallization. A similar mechanism has been proposed to explain sectoral chemical (Ge, Ag) zoning in sphalerite (Barbanson and Geldron 1983). According to Pough (1940) and Kostov (1968), the main faces of willemite prisms are $\{110\}$, $\{101\}$, $\{012\}$, and $\{001\}$. While the first one is characteristic of fibrous habits (e.g., Wil Ib), the three other one are frequent in prismatic crystals (e.g., Wil Ia). The comparison of the surface atomic structure of the different faces shows that all faces except $\{012\}$ display alternating Zn and Si, with various Si/Zn ratios. However, the $\{012\}$ surface is a continuous plane of Si ions, which was much more favorable for Ge incorporation. Therefore, the incorporation of Ge in Wil Ia is limited by willemite crystal growth, while its introduction in Wil Ib depends on the chemical composition of the fluids, which controls the element variation of oscillatory-zoned crystals (Shore and Fowler 1996). Oscillatory growth zoning in willemite is frequently described in the literature (Coppola et al. 2008; Terracciano 2008; Saini-Eidukat et al. 2009, 2016), but it is the first time that sector zoning is reported for this mineral. Growth sectors defined by the faces on which the growth took place are characterized by variable Ge and Pb contents (Fig. 8). While Ge-rich bright sectors $\{012\}$ have low Pb contents, higher Pb concentration is found in Ge-poor dark sectors $\{101\}$, $\{110\}$, or $\{001\}$.

Spectral analysis curves are characterized by a maximum of intensity at 460–480 nm (Fig. 11), in agreement with the blue luminescence observed under the microscope (Fig. 6). The experimental curves from Bou Arhous willemite significantly differ from those given by pure willemite (Randall

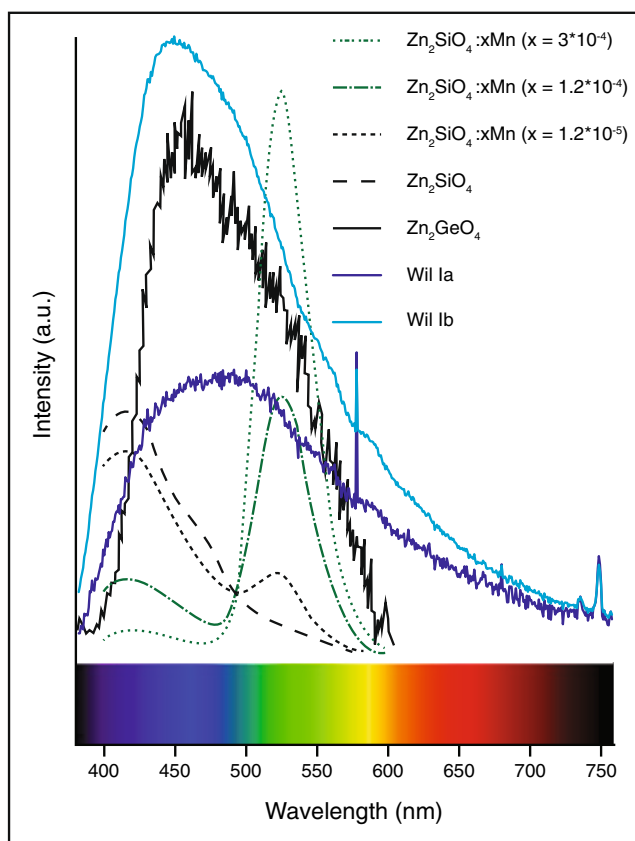


Fig. 11 Luminescence spectra of two observed areas dominated by Wil Ia or Wil Ib. The curves of variously Mn-doped willemite (Leverenz 1950) and of a synthetic Ge analog of willemite (Zn_2GeO_4 , Tsai et al. 2008) are shown for comparison

1938; Yang et al. 2004) or Mn-doped willemite (Leverenz 1950) but are very similar to that obtained by analyzing synthetic Zn_2GeO_4 nanorods (Tsai et al. 2008). Zinc germanate has a crystal structure similar to that of willemite (Hang et al. 1970). The obvious correlation between the Ge content and the intensity of luminescence is only valid for Wil Ia crystals, and no similar observation was made for Wil Ib. Therefore, it is difficult to ascertain the role of activator ion for Ge^{4+} . Alternative processes could be envisaged: (i) quenching by ions with intense charge transfer bands like Fe^{2+} (Terracciano 2008), (ii) sensitizing of Mn by ions with intensive absorption bands like Pb^{2+} (Carpenter and Vicenzi 2012), (iii) luminescence caused by defect activators, such as interstitial Pb^{2+} (Yang et al. 2004; Takahashi et al. 2010), or (iv) other luminescence centers (e.g., Ti^{4+} , Eu^{2+} , Ce^{3+} , Hf^{4+}) not detected by the used analytical methods but recognized as activators for the blue luminescence (see a review in Takesue et al. 2009).

Nature of the mineralizing fluids involved

The host rock carbonates of the Bou Arhous mineralization have $\delta^{13}\text{C}$ values in a range from -1.7 to 1.4 ‰ (Table 3),

similar to those of Pliensbachian limestone (0.5 to 2.9 ‰) hosting the Bou Dahar Zn-Pb mineralization, 75 km to the west of Bou Arhous (Rddad and Bouhleb 2016). The $\delta^{18}\text{O}$ values of carbonates (22.9 to 24.1 ‰) are also similar to those of Bou Dahar (22.7 to 25.7 ‰). Such $\delta^{13}\text{C}$ and $\delta^{18}\text{O}$ values are within the range of marine Jurassic limestones (Veizer and Hoefs 1976).

Carbon stable isotope ratios of cerussite are similar to those measured for supergene ores from Iglesias, Broken Hill and deposits in Eastern Belgium (see a review in Gilg et al. (2008); Fig. 12a). The $\delta^{13}\text{C}$ (between -11 and -15.1 ‰) values are lower than the typical values of cerussite from marine slags (0 ± 2 ‰) given by Gilg et al. (2008). The ^{13}C -depleted carbon component can be explained by either contributions of carbon from soil CO_2 related to respiration of C3 plants (Cerling 1984) or organic carbon issued from the activity of sulfide-oxidation bacteria (Melchiorre and Enders 2003). The average $\delta^{18}\text{O}$ value (12.1 ‰, $n = 4$) of cerussite is lower than that obtained in supergene deposits (15 to 20 ‰) or from marine slags (17.9 ‰, Gilg et al. 2008) but similar to that of the Garpenberg deposit, Sweden (11.6 ‰; Vivallo and Broman 1993) or to that of Badenweiler in the Schwarzwald mining district (11.2 to 15.6 ‰, Hassler et al. 2014). These low values may be explained by either isotopically lighter water or by higher temperatures of formation. The absence of any correlation between carbon and oxygen isotope values of cerussite suggests that dissolution of the host limestone cannot only account for the source of carbonate in cerussite.

At present, the oxygen isotope composition of willemite was only reported from Sterling Hill (USA) and Vazante (Brazil), with respective isotopic compositions between 7.4 and 11.4 ‰ and between 10.9 and 13.8 ‰ (Johnson et al. 1990; Monteiro et al. 1999). In addition to fluid inclusions that recorded salinities of 3–15 wt% eq. NaCl and homogenization temperatures between 120 and 175 °C (Dardenne and Freitas-Silva 1999), Monteiro et al. (1999) recalculated a temperature range (from 263 to 294 °C) at the time of mineralization using the stable isotope composition of cogenetic mineral pairs. Therefore, they recalculated the oxygen isotope composition of the fluid in equilibrium with willemite, using the theoretical fractionation equation between willemite and water (Zheng 1993).

$$1000 \ln \alpha_{\text{wil-wat}} = 3.79(10^6/T^2) - 8.94(10^3/T) + 2.5 \quad (1)$$

The range of oxygen isotope compositions ($\delta^{18}\text{O} = 12$ to 14 ‰) of the fluid (Fig. 12b) led Appold and Monteiro (2009) to propose a mixing process between hot, saline, reducing, acidic fluids and cool, oxidizing meteoric waters; precipitation results from an increase in pH and/or a small decrease in the temperature (Brugger et al. 2003). Mixing of hydrothermal fluids with seawater was also hypothesized for explaining

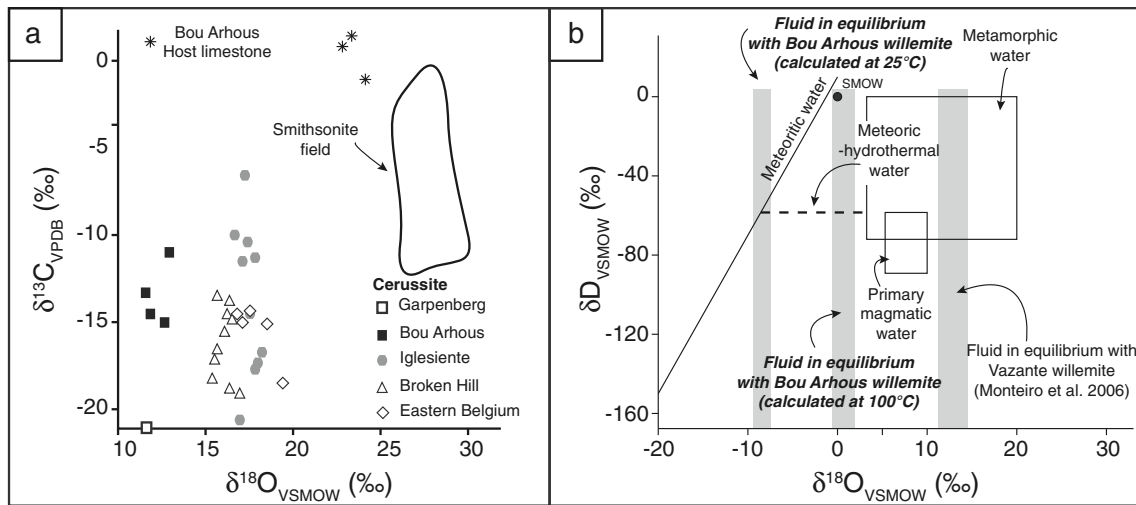


Fig. 12 **a** Carbon and oxygen isotope compositions of cerussite and host limestone from the Bou Arhous deposit. Data from other deposits are taken from Gilg et al. (2008) and references herein. **b** Hydrogen and oxygen isotope compositions of supergene (25 °C) and low-temperature

(100 °C) hydrothermal fluids in equilibrium with Bou Arhous willemite. The isotope composition of fluids in equilibrium with hypogene willemite from Vazante, Brazil (Monteiro et al. 1999) is shown for comparison

the isotopic compositions of Sterling Hill rocks and ores (Johnson et al. 1990).

The oxygen isotope composition of Bou Arhous willemite is characterized by $\delta^{18}\text{O}$ values ranging between 5.3 and 7.8 ‰ (Table 3), significantly lower than those measured for Vazante or Sterling Hill. The large range of oxygen isotope values (2.5 ‰) may also indicate that fluid mixing was involved during the precipitation of willemite or that willemite precipitated at different temperatures. The study of fluid inclusions in willemite from Bou Arhous was not conclusive, with only monophasic inclusions observed. This suggests that the temperatures of the Tertiary fluids responsible for willemite formation were below 130 °C (e.g., Gilg et al. 2014). The established paragenetic succession shows a first-order contemporaneity of willemite and cerussite (Fig. 9). Using equation (Eq. 1) and the oxygen isotope fractionation equation between cerussite and water (Eq. 2; Gilg et al. 2008), it is possible to calculate the equilibrium temperature between the willemite-cerussite pairs (BA117, BA118, and BA134).

$$1000\ln\alpha_{\text{cer-wat}} = 2.29(10^6/T^2) - 3.56 \quad (2)$$

After discarding the negative solutions, the obtained temperatures range from 237 to 343 °C. While these temperatures are similar to those proposed in hypogene willemite deposits (e.g., Vazante; Monteiro et al. 1999), the local geological setting of Bou Arhous deposit totally differs from the structural and paragenetic characteristics of hypogene deposits, without carbonatization and hematite alteration (Hitzman et al. 2003). In addition, such temperatures are too high for cerussite, a mineral exclusively reported in the supergene stages of ore deposits, although high temperature (up to 240 °C)

experiments on cerussite were made by O’Neil et al. (1969). Cerussite and willemite are not in isotopic equilibrium and thus not cogenetic. They precipitated from at least two fluids with different oxygen isotope compositions or formed at different temperatures. The successive bands of cerussite and willemite (Fig. 5f) rather support the hypothesis of different fluids involved in the precipitation of both minerals.

Supergene versus low-temperature hypogene willemite

Based on the present data, it is not possible to ascertain the origin of willemite at Bou Arhous. The geological features of the deposits suggest a supergene origin of the non-sulfide mineralization and therefore low temperatures (around 25 °C) could be assumed. Such a temperature corresponds to that presently recorded in the karst cavities hosting the mineralization. Synthetic willemite was obtained at room temperature by sol–gel methods and occurs as small spheres or aggregates (Esquevin 1960; Takesue et al. 2009). Thermodynamic modeling also showed that willemite may form at 25 °C under high pH, high silica activity, and low CO₂ partial pressure conditions (Brugger et al. 2003). The oxygen isotopic composition of the paleowater was calculated at 25 °C, using the bond-strength theory equation for isotope fractionation between willemite and water (Eq. 1; Zheng 1993). The obtained isotopic compositions for the paleowater (Table 3) plot close to the meteoric line (Craig 1961), although no constrain on the vertical axis (δD) is available (Fig. 12b). The computed $\delta^{18}\text{O}$ values for the paleofluid have a range between -9.3 and -7.4 ‰ (Table 3), lower than the average value (-7.5 ‰) of present-day precipitations at Bab Bou Idir, northern Morocco (Ouda et al. 2005). This difference could be explained by

differences in altitude and climate between the Bab Bou Idir station and the Bou Arhous range during the Tertiary.

Alternatively, low-temperature hydrothermal fluids (<130 °C) may have been involved in the formation of willemite. Such fluids have been hypothesized for the origin of willemite in the deposits of Eastern Belgium (Coppola et al. 2008). In the case of Bou Arhous, the absence of isotopic equilibrium between cerussite and willemite and the relatively large range of isotopic compositions for willemite suggest the involvement of at least two fluids and their mixing. Together with supergene water, hydrothermal fluids have also contributed to the formation of the non-sulfide ore. As temperature is the main parameter controlling the precipitation of willemite instead of hemimorphite (McPhail et al. 2003, 2006), temperatures over 90–100 °C are required, in agreement with the presence of monophasic inclusions ($T < 130$ °C). Assuming a temperature of 100 °C, we recalculated a range of isotopic compositions for the paleofluid between -0.5 and 2 ‰ (Table 3). The data fall into an intermediate domain between the deep fluid fields and the supergene line, in agreement with the mixing hypothesis (Fig. 12b).

Whatever the hypothesis, high silica activity is necessary to prevent the precipitation of smithsonite and hydrozincite, which are only reported in few samples in the Bou Arhous deposit (Leblanc 1968). The source of silica is thus a crucial issue. Like in Eastern Belgium (Coppola et al. 2008), few present-day hot springs are currently known in the area, especially to the west of Bou Arhous (Bahaj et al. 2013). In addition, the hydrochemical study of the underground waters in the Zizi and Guir basins, to the south of the Bou Arhous range, shows that the present-day water within the Sinemurian limestone is a calcic bicarbonate type; their extremely high silica contents (up to 5000 mg/L) are interpreted as the result of a long residence time of the waters and/or an important mixture with thermal waters (Bahaj et al. 2013). A local source for silica cannot be excluded too and may even be indicated by the partial dissolution of the idiomorphic quartz crystals present in the micritic limestone (Fig. 3). Although the dissolution rate of quartz is low at low temperatures (Dove 1994), long-lived weathering since the Tertiary and undersaturation of the karst waters may partly contribute to a slow but non-negligible enrichment in silica. An alternative local source of Si could be the residual clays of the karst, mainly composed of illite, kaolinite, and smectite (Buatier et al. 2016; Choulet et al. 2016).

Conclusion

The Bou Arhous deposit in the Moroccan High Atlas is characterized by willemite ore. Several generations of willemite spatially and temporally associated with cerussite were distinguished based on different criteria including crystal shape, zoning type, and major and trace element contents. Based on

oxygen stable isotope data of bulk mineral fractions, cerussite and willemite are not in isotope equilibrium and therefore were not cogenetic, requiring different fluid compositions for their formation. In addition to a contribution of supergene water, low-temperature (<130 °C) hydrothermal fluids buffered by the country rocks may have been involved. The input of hydrothermal fluids is probably responsible for the high silica activity, which is necessary to precipitate willemite instead of zinc carbonates, especially within carbonate host rocks. A local contribution by the silicate minerals of the host limestone cannot be excluded though. Further work on willemite is required to verify the conditions of formation; stable oxygen isotope compositions of the different generations of willemite and cerussite could help to understand the evolution of mineralizing fluids.

The Bou Arhous willemite may contain up to several thousands of parts per million of Ge. The Ge content in willemite, related to the Si-Ge substitution, is controlled by the crystal morphology in the case of sector zoning. Since the Ge content of sulfide minerals is low (less than 100 ppm), it is hypothesized that hydrothermal fluids, responsible for the formation of willemite, also transported Ge in part. In the present context of Ge criticality, willemite ores may therefore represent an interesting target for exploration (Höll et al. 2007; EU Commission 2014).

Acknowledgments The authors are indebted to Managem Company for providing access to the Bou Arhous Mine. They thank Didier Convert-Gaubier for thin-section preparation, as well as Aurélien Eglinger and Philippe Goncalves from Chrono-Environnement for LA-ICP-MS data acquisition and Martin Robyr, Evelyne Tomare, and Anne-Cécile Hauser from the University of Lausanne for EPMA data acquisition. They also warmly acknowledge the assistance of Benita Putlitz with oxygen isotope measurements on the silicate line at UNIL. This study has benefited from a financial support by of Région Franche-Comté with the 2014 “Argzinc” Franco-Suisse project. Access to SEM facilities of the MIMENTO center was made in the frame of cooperative projects in the Renatech network. Two anonymous reviewers, Associate Editor Albert Gilg, and Editor-in-Chief Bernd Lehmann are acknowledged for their constructive remarks that helped to improve the manuscript.

References

- Appold MS, Monteiro LVS (2009) Numerical modeling of the hydrothermal zinc silicate and sulfide mineralization in the Vazante deposit, Brazil. *Geofluids* 9:96–115
- Bahaj T, Kacimi I, Hilali M, Kassou N, Mahboub A (2013) Preliminary study of the groundwater geochemistry in the sub-desert area in Morocco: case of the Ziz-Ghris basins. *Proced Earth Planet Sci* 7: 44–48
- Barbanson L, Geldron A (1983) Distribution du germanium, de l'argent et du cadmium entre les schistes et les minéralisations stratiformes et filoniennes à blende-sidérite de la région de Saint-Salvy (Tam). *Chron Rech Min* 470:33–42
- Belissont R, Boiron M-C, Luais B, Cathelineau M (2014) LA-ICP-MS analyses of minor and trace elements and bulk Ge isotopes in zoned Ge-rich sphalerites from the Noailhac–Saint-Salvy deposit (France):

- insights into incorporation mechanisms and ore deposition processes. *Geochim Cosmochim Acta* 126:518–540
- Bernstein LR (1985) Germanium geochemistry and mineralogy. *Geochim Cosmochim Acta* 49:2409–2422
- Bernstein LR (1986) Geology and mineralogy of the APEX germanium–gallium mine, Washington County, Utah. *US Geol Surv Bull* 1577: 1–9
- Bhalla RJRSB, White EW (1972) Cathodoluminescence characteristics of Mn^{2+} activated willemite (Zn_2SiO_4) single crystals. *J Electrochem Soc* 119:740–743
- Boni M, Large DE (2003) Nonsulfide zinc mineralization in Europe: an overview. *Econ Geol* 98:715–729
- Boni M, Mondillo N (2015) The “calamines” and the “others”: the great family of supergene nonsulfide zinc ores. *Ore Geol Rev* 67:208–233
- Boni M, Coppola V, Dejonghe L, Fedele L (2005) Willemite in the Belgian non-sulphide deposits: a fluid inclusion study. *Period Miner* 73:1–14
- Boni M, Gilg HA, Balassone G, Schneider J, Allen CR, Moore F (2007) Hypogene Zn carbonate ores in the Angouran deposit, NW Iran. *Mineral Deposita* 42:799–820
- Boni M, Terracciano R, Balassone G, Gleeson SA, Matthews A (2011) The carbonate-hosted willemite prospects of the Zambezi Metamorphic Belt (Zambia). *Mineral Deposita* 46:707–729
- Brunner J, McPhail DC, Wallace M, Waters J (2003) Formation of willemite in hydrothermal environments. *Econ Geol* 98:819–835
- Buatier M, Choulet F, Petit S, Chassagnon R, Vennemann T (2016) Nature and origin of natural Zn clay minerals from the Bou Arhous Zn ore deposit: evidence from electron microscopy (SEM-TEM) and stable isotope compositions (H and O). *App Clay Sci*. doi:10.1016/j.clay.2016.07.004
- Carpenter P, Vicenzi E (2012) A combined EPMA and cathodoluminescence study of minerals from Franklin NJ. *Microsc Microanal* 18(S2):1746–1747
- Cerling TE (1984) The stable isotopic composition of modern soil carbonate and its relationship to climate. *Earth Planet Sci Letts* 71:229–240
- Charles N, Choulet F, Sizaret S, Chen Y, Barbanson L, Ennaciri A, Badra L, Branquet Y (2016) Internal structures and dating of non-sulphide Zn deposits using rock magnetism: insights from the Moroccan High Atlas. *Mineral Deposita* 51:151–175
- Choulet F, Charles N, Barbanson L, Branquet Y, Sizaret S, Ennaciri A, Badra L, Chen Y (2014) Non-sulfide zinc deposits of the Moroccan High Atlas: multi-scale characterization and origin. *Ore Geol Rev* 56:115–140
- Choulet F, Buatier M, Barbanson L, Guégan R, Ennaciri A (2016) Zinc-rich clays in supergene non-sulfide zinc deposits. *Mineral Deposita* 51:467–490
- Cook NJ, Ciobanu CL, Pring A, Skinner W, Shimizu M, Danyushevsky L, Saini-Eidukat B, Melcher F (2009) Trace and minor elements in sphalerite: a LA-ICPMS study. *Geochim Cosmochim Acta* 73: 4761–4791
- Coppola V, Boni M, Gilg HA, Balassone G, Dejonghe L (2008) The “calamine” nonsulfide Zn–Pb deposits of Belgium: petrographical, mineralogical and geochemical characterization. *Ore Geol Rev* 33: 187–210
- Craig H (1961) Isotopic variations in meteoric waters. *Science* 133:1702–1703
- Daliran F, Pride K, Walther J, ZA B, RJ B (2013) The Angouran Zn (Pb) deposit, NW Iran: evidence for a two stage, hypogene zinc sulfide–zinc carbonate mineralization. *Ore Geol Rev* 53:373–402
- Dardenne MA, Freitas-Silva FH (1999) Pb–Zn ore deposits of Bambuí and Vazante groups, in the São Francisco Craton and Brasília Fold Belt, Brazil. In: Silva MG, Misi A (eds) Base metal deposits of Brazil. *MME7CPRM/DNPM, Belo Horizonte*, pp. 75–83
- Dejonghe L (1998) Zinc-lead deposits of Belgium. *Ore Geol Rev* 12: 329–354
- Dove PM (1994) The dissolution kinetics of quartz in sodium chloride solutions at 25 degrees to 300 degrees C. *Am J Sci* 294:665–712
- Esquevin J (1960) Les silicates de zinc, étude de produits de synthèse et des minéraux naturels. Institut National de la Recherche Agronomique, Saint-Amand in French
- EU Commission (2014) Critical raw materials for the EU. Report of the Ad-hoc Working Group on Defining Critical Raw Materials. Brussels, Belgium
- Flügel E (2010) *Microfacies of carbonate rocks*, 2nd edn. Springer-Verlag, Berlin-Heidelberg
- Frizon de Lamotte D, Saint-Bezard B, Bracene E, Mercier E (2000) The two main steps of the atlas building and geodynamics of the western Mediterranean. *Tectonics* 19:740–761
- Gilg HA, Struck U, Vennemann T, Boni M (2003) Phosphoric acid fractionation for smithsonite and cerussite between 25 and 72 °C. *Geochim Cosmochim Acta* 67:4049–4055
- Gilg HA, Boni M, Hochleitner R, Struck U (2008) Stable isotope geochemistry of carbonate minerals in supergene oxidation zones of Zn–Pb deposits. *Ore Geol Rev* 33:117–133
- Gilg HA, Krüger Y, Taubald H, van den Kerkhof AM, Frenz M, Morteani G (2014) Mineralisation of amethyst-bearing geodes in Ametista do Sul (Brazil) from low-temperature sedimentary brines: evidence from monophase liquid inclusions and stable isotopes. *Mineral Deposita* 49:861–877
- Groves I, Carman CE, Dunlap WJ (2003) Geology of the Beltana willemite deposit, Flinders Ranges, South Australia. *Econ Geol* 98: 797–818
- Hang C, Simonov MA, Belov NV (1970) Crystal structures of willemite $Zn_2(SiO_4)$ and its germanium analog $Zn_2(GeO_4)$. *Sov Phys Crystallogr USSR* 15:387–390
- Hassler K, Taubald H, Markl G (2014) Carbon and oxygen isotope composition of Pb-, Cu- and Bi-carbonates of the Schwarzwald mining district: carbon sources, first data on bismutite and the discovery of an oxidation zone formed by ascending thermal water. *Geochim Cosmochim Acta* 113:1–16
- Hitzman MW, Reynolds NA, Sangster DF, Allen CR, Carman CE (2003) Classification, genesis, and exploration guides for nonsulfide zinc deposits. *Econ Geol* 98:685–714
- Höll R, Kling M, Schroll E (2007) Metallogensis of germanium—a review. *Ore Geol Rev* 30:145–180
- Ito J, Frondel C (1967) Synthesis of lead silicates: larsenite, barysilite and related phases. *Am Mineral* 52:1077–1084
- Johnson CA, Rye DM, Skinner BJ (1990) Petrology and stable isotope geochemistry of the metamorphosed zinc-iron-manganese deposit at Sterling Hill. New Jersey: *Econ Geol* 85:1133–1161
- Kasemann S, Meixner A, Rocholl A, Vennemann T, Schmitt A, Wiedenbeck M (2001) Boron and oxygen isotope composition of certified reference materials NIST SRM 610/612, and reference materials JB-2G and JR-2G. *Geostand Newslett* 25:405–416
- Klaska K-H, Eck JC, Pohl D (1978) New investigation of willemite. *Acta Crystallogr B* 34:3324–3325
- Kostov I (1968) Habit types and genesis of phenakite and willemite. *Krist Techn* 3:629–636
- Laville E, Piqué A (1991) La distension crustale atlantique et atlasique au Maroc au début du Mésozoïque: le rejeu des structures hercyniennes. *Bull Soc Geol Fr* 162:1161–1171
- Leblanc M (1968) Étude géologique et métallogénique du Jbel Bou-Arhous et de son prolongement oriental (Haut Atlas marocain oriental). *Not Mem Serv Geol Maroc* 206:117–206
- Leverenz HW (1950) *An introduction to luminescence of solids*. John Wiley & Sons, New York
- Lombaard AF, Günzel A, Innes J, Krüger TL (1986) The Tsumeb lead-copper-zinc-silver deposit, south west Africa/Namibia. In: Anhaeusser CR, Maske S (eds) *Mineral deposits of southern Africa*. Geological Society of South Africa, Johannesburg, pp. 1761–1787

- Lukić DM, Petrović DMD, Mitrić M, Đaćanin L (2008) Optical and structural properties of $\text{Zn}_2\text{SiO}_4\text{:Mn}^{2+}$ green phosphor nanoparticles obtained by a polymer-assisted sol–gel method. *Scr Mater* 58:655–658
- Lüning S, Loydell DK, Sutcliffe O, Ait Salem A, Archer R, Zanella E, Craig J, Harper DAT (2000) Silurian - lower Devonian black shales in Morocco: where are the organically richest horizons? *J Petrol Geol* 23:293–311
- McPhail DC, Summerhayes E, Welch S, Brugger J (2003) The geochemistry of zinc in the regolith. In: Roach IC (ed) *Advances in regolith. CRC for Landscape Environments and Mineral Exploration*, pp. 287–291
- McPhail DC, Summerhayes E, Jayaratne V, Christy A (2006) Hemimorphite solubility and stability of low-T zinc minerals. *Geochim Cosmochim Acta* 70:A414
- Melcher F, Saini-Eidukat B, Göttlicher J, Steininger R, Cook N, Ciobanu C (2009) Germanium in sphalerite and willemite at the Tres Marias mine, Mexico: An EMPA, CL, LA-ICP-MS and synchrotron study. In: *Hallesches Jahrbuch für Geowissenschaften. DMG-Tagung 2009*, Halle, pp. 163
- Melchiorre EB, Enders MS (2003) Stable isotope geochemistry of copper carbonates at the Northwest Extension deposit, Morenci district, Arizona: implications for conditions of supergene oxidation and related mineralization. *Econ Geol* 98:607–621
- Melcher F, Oberthür T, Vetter U, Gross C, Vollbrecht A, Brauns M, Haack U. 2003. Germanium in carbonate-hosted Cu–Pb–Zn mineralization in the Otavi Mountain Land, Namibia. In: Eliopoulos D. (Ed.), *Mineral Exploration and Sustainable Development*. Millpress, Rotterdam, pp. 701–704
- Monteiro LVS, Bettencourt JS, Spiro B, Graca R, Oliveira TF (1999) The Vazante zinc mine. Minas Gerais, Brazil: constraints on willemite mineralization and fluid evolution: *Explor Min Geol* 8:21–42
- Monteiro LVS, Bettencourt JS, Juliani C, Oliveira TF (2006) Geology, petrography, and mineral chemistry of the Vazante non-sulfide and Ambrosia and Fagundes sulfide-rich carbonate-hosted Zn(Pb) deposits, Minas Gerais, Brazil. *Ore Geol Rev* 28:201–234
- Monteiro LVS, Bettencourt JS, Juliani C, Oliveira TF (2007) Nonsulfide and sulfide-rich zinc mineralizations in the Vazante, ambrosia and Fagundes deposits, Minas Gerais, Brazil: mass balance and stable isotope characteristics of the hydrothermal alterations. *Gondwana Res* 11:362–381
- Mouguina EM (2004) Les minéralisations polymétalliques (Zn–Pb, Cu, Co, Ni) du Jurassique du Haut Atlas central (Maroc): Contexte géodynamique, typologies et modèles génétiques. *Dissertation, Faculté des Sciences Semlalia de Marrakech*
- O’Neil JR, Clayton RN, Mayeda TK (1969) Oxygen isotope fractionation in divalent metal carbonates. *J Chem Phys* 51:5547–5558
- Ouda B, El Hamdaoui A, Ibn Majah M (2005) Isotopic composition of precipitation at three Moroccan stations influenced by oceanic and Mediterranean air masses. In: *Isotopic composition of precipitation in the Mediterranean Basin in relation to air circulation patterns and climate*. IAEA, Vienna TECDOC-1453:125–140
- Palache C (1928) Phosphorescence and fluorescence of Franklin minerals. *Am Mineral* 13:330–333
- Palache C (1935) The minerals of Franklin and Sterling Hill, Sussex County, New Jersey. *US Geol Surv Prof Pap* 180, USGS, Washington
- Pearce NJG, Perking WT, Westgate JA, Gorton MP, Jackson SE, Neal CR, Chenery SP (1997) A compilation of new and published major and trace element data for NIST SRM 610 and NIST SRM 612 glass materials. *Geostand Newslett* 21:115–144
- Pokrovski GS, Roux J, Hazemann J-L, Testemale D (2005) An X-ray absorption spectroscopy study of argutite solubility and germanium aqueous speciation in hydrothermal fluids to 500 °C and 400 bar. *Chem Geol* 217:127–145
- Pough FH (1940) Willemite morphology and paragenesis at Balmat, New York. *Am Mineral* 25:488–496
- Pough FH (1941) Occurrence of willemite. *Am Mineral* 26:92–102
- Randall JT (1938) Luminescence of solids at low temperatures. *Nature* 142:113–114
- Rddad L, Bouhlef S (2016) The Bou Dahar Jurassic carbonate-hosted Pb–Zn–Ba deposits (Oriental High Atlas, Morocco): fluid-inclusion and C–O–S–Pb isotope studies. *Ore Geol Rev* 72:1072–1087
- Reichert J, Borg G (2008) Numerical simulation and a geochemical model of supergene carbonate-hosted non-sulphide zinc deposits. *Ore Geol Rev* 33:134–151
- Rosenbaum J, Sheppard SMF (1986) An isotopic study of siderites, dolomites and ankerites at high temperatures. *Geochim Cosmochim Acta* 50:1147–1150
- Rouvier H, Perthuisot V, Mansouri A (1985) Pb–Zn deposits and salt-bearing diapirs in Southern Europe and North Africa. *Econ Geol* 80:666–687
- Saini-Eidukat B, Melcher F, Lodziak J (2009) Zinc-germanium ores of the Tres Marias mine, Chihuahua, Mexico. *Mineral Depos* 44:363–370
- Saini-Eidukat B, Melcher F, Göttlicher J, Steininger R (2016) Chemical environment of unusually Ge- and Pb-rich willemite, Tres Marias Mine, Mexico. *Minerals* 6:20. doi:10.3390/min6010020
- Sheffer HW (1966) The occurrence of germanium in willemite. *Geochim Cosmochim Acta* 30:837–838
- Shore M, Fowler AD (1996) Oscillatory zoning in minerals: a common phenomenon. *Can Mineral* 34:1111–1126
- Spötl C, Vennemann TW (2003) Continuous-flow isotope ratio mass spectrometric analysis of carbonate minerals. *Rapid Commun Mass Spectrom* 17:1004–1006
- Swart PK, Burns SJ, Leder JJ (1991) Fractionation of the stable isotopes of oxygen and carbon during reaction of calcite with phosphoric acid as a function of temperature and method. *Chem Geol* 86:89–96
- Takahashi Y, Ando M, Iwasaki K, Masai H, Fujiwara T (2010) Defect activation in willemite-type Zn_2GeO_4 by nanocrystallization. *Appl Phys Lett*. doi:10.1063/1.3481081
- Takesue M, Hayashi H, Smith RL (2009) Thermal and chemical methods for producing zinc silicate (willemite): a review. *Prog Cryst Growth Char Mat* 55:98–124
- Terracciano R (2008) Willemite mineralisation in Namibia and Zambia. *Dissertation, Università degli Studi di Napoli Federico II*
- Tsai MY, Yu CY, Wang CC, Perng TP (2008) Water-driven formation of luminescent Zn_2GeO_4 nanorods from Zn-containing Ge nanoparticles. *Cryst Growth Des* 8:2264–2269
- Veizer J, Hoefs J (1976) Nature of $\text{O}^{18}/\text{O}^{16}$ and $\text{C}^{13}/\text{C}^{12}$ secular trends in sedimentary carbonate rocks. *Geochim Cosmochim Acta* 40:1387–1395
- Vivallo W, Broman C (1993) Genesis of the earthy ores at Garpenberg, south central Sweden. *Geol Foren Stockh Föhr* 115:209–214
- Yang P, Lu MK, Song CF, Liu SW, Gu F, Wang SF (2004) Photoluminescence of Pb^{2+} ions in sol–gel derived Zn_2SiO_4 . *Inorg Chem Comm* 7:268–270
- Zheng YF (1993) Calculation of oxygen isotope fractionation in anhydrous silicate minerals. *Geochim Cosmochim Acta* 57:1079–1109